

## RESEARCH LETTER

10.1002/2015GL065911

## Key Points:

- Boundary cloud variations at seasonal and centennial scales are correlated
- Boundary cloud seasonal response is correlated with sensitivity
- Observations suggest a higher climate sensitivity than multimodel mean

## Supporting Information:

- Figure S1

## Correspondence to:

C. Zhai,  
chengxing.zhai@jpl.nasa.gov

## Citation:

Zhai, C., J. H. Jiang, and H. Su (2015), Long-term cloud change imprinted in seasonal cloud variation: More evidence of high climate sensitivity, *Geophys. Res. Lett.*, 42, 8729–8737, doi:10.1002/2015GL065911.

Received 25 AUG 2015

Accepted 1 OCT 2015

Accepted article online 5 OCT 2015

Published online 24 OCT 2015

## Long-term cloud change imprinted in seasonal cloud variation: More evidence of high climate sensitivity

Chengxing Zhai<sup>1</sup>, Jonathan H. Jiang<sup>1</sup>, and Hui Su<sup>1</sup>
<sup>1</sup>Jet Propulsion Laboratory, California Institute of Technology, Pasadena, California, USA

**Abstract** The large spread of model equilibrium climate sensitivity (ECS) is mainly caused by the differences in the simulated marine boundary layer cloud (MBLC) radiative feedback. We examine the variations of MBLC fraction in response to the changes of sea surface temperature (SST) at seasonal and centennial time scales for 27 climate models that participated in the Coupled Model Intercomparison Project phase 3 and phase 5. We find that the intermodel spread in the seasonal variation of MBLC fraction with SST is strongly correlated with the intermodel spread in the centennial MBLC fraction change per degree of SST warming and that both are well correlated with ECS. Seven models that are consistent with the observed seasonal variation of MBLC fraction with SST at a rate  $-1.28 \pm 0.56\%/K$  all have ECS higher than the multimodel mean of 3.3 K yielding an ensemble-mean ECS of 3.9 K and a standard deviation of 0.45 K.

## 1. Introduction

Large intermodel disagreement in equilibrium climate sensitivity (ECS), the global-mean surface temperature change in response to the doubling of CO<sub>2</sub>, has persisted for decades [Arrhenius, 1896; Callendar, 1938; Charney et al., 1979; Meehl et al., 2007; Stocker et al., 2013]. Although cloud feedback with a primary contribution from marine boundary layer clouds (MBLC) has been identified as a leading factor that causes the large spread in model ECS [Cess et al., 1990; Bony and Dufresne, 2005; Andrews et al., 2012; Zelinka et al., 2012], constraining and improving the simulations of cloud feedback in general circulation models (GCMs) remain a challenge. Recently, a number of studies demonstrated that there exist quantities in present-day climate simulations linked to cloud feedback in future climate change. Constraining these quantities using observations thus provides practical means to constrain ECS [Fasullo and Trenberth, 2012; Klein et al., 2013; Sherwood et al., 2014; Su et al., 2014; Tian, 2015].

All these emergent constraints are based on the multiyear mean climate states simulated in the models, including mean relative humidity, cloud fraction, circulation strength, and precipitation bias. An unanswered question is why climatological mean states bear any relations to future cloud changes in response to surface warming. Intuitively, one would expect the physical processes that govern cloud changes on long time scale, such as centennial time scale of 100 years or more, to be equally active on shorter time scales, given that the response time of atmospheric dynamic and radiative processes related to clouds is on the order of hours to days. Thus, there have been studies that examined short-term cloud feedback on the interannual and decadal time scales [Dessler, 2010; Clement et al., 2009] to gain insights into cloud feedback for long-term climate change. Based on the similarities in tropic environmental changes between seasonal variation and global warming, Fasullo and Trenberth [2012] used relative humidity to constrain the model ECS. Tsushima et al. [2013] found that the models that best capture the seasonal variations of cloud regimes tend to have higher climate sensitivity. The relationship between the seasonal and long-term variations of clouds with sea surface temperature (SST), however, has not been established despite the seasonal variation of clouds that has been well observed [Klein and Hartmann, 1993], and a strong correlation of snow albedo feedback on the seasonal time scale and in the climate change context was reported for models [Hall and Qu, 2006]. This study aims to fill the gap to establish a linkage between seasonal cycle and cloud changes at centennial time scale, with a particular focus on the MBLC fraction, one of the most important parameters that determine the shortwave cloud radiative feedback. Once the linkage is established, the observations of seasonal variation of MBLC are used to discriminate the low cloud shortwave feedback and thus models' ECS. Unlike previous studies that used climatological mean states to constrain ECS, this study tackles the seasonal variabilities in current climate and their relevance to long-term climate change.

**Table 1.** Horizontal Resolutions, Vertical Levels, ECS, and Number of Levels Below 700 hPa for the 16 CMIP5 and 11 CMIP3 Models Used in This Study

CMIP Phase	Modeling Center Acronym—Model Name	Resolution (Longitude × Latitude × Levels)	ECS (K)	Number of Levels Below 700 hPa
CMIP3	CCCMA-cgcm3.1	3.75° × 3.6802°, L31	3.4	15
CMIP3	GISS-e-r	5° × 3°, L17	2.7	5
CMIP3	IAP-fgoals1	2.8125° × 6.1315°, L26	2.3	6
CMIP3	INM-cm3	5° × 4°, L21	2.1	7
CMIP3	IPSL-cm4	3.75° × 2.5352°, L19	4.4	6
CMIP3	MIRCO-medres	2.8125° × 2.7673°, L20	4.0	6
CMIP3	MPI-cham5	1.875° × 1.849°, L31	3.4	9
CMIP3	MRI-cgcm2	2.8125° × 2.7673°, L17	3.2	4
CMIP3	NCAR-ccsm	1.4062° × 1.389°, L26	2.7	6
CMIP3	NCAR-pcm1	2.8125° × 2.7673°, L18	2.1	6
CMIP3	UKMO-hadcm3	3.75° × 2.5°, L19	3.3	6
CMIP5	CCCMA-canesm2	2.8125° × 2.79°, L35	3.69	15
CMIP5	CNRM-cm5a	1.40625° × 1.4°, L31	3.25	9
CMIP5	CSIRO-QCCCE-mk3.6	1.875° × 1.86°, L18	4.08	7
CMIP5	GFDL-cm3	2.5° × 2°, L48	3.97	12
CMIP5	GISS-e2-h	2.5° × 2°, L29	2.30	9
CMIP5	GISS-e2-r	2.5° × 2°, L29	2.11	9
CMIP5	IAP-fgoals-g2	2.8125° × 6.1315°, L26	3.45	6
CMIP5	INM-cm4	2° × 1.5°, L21	2.08	7
CMIP5	IPSL-cm5a	3.75° × 1.8947°, L39	4.13	9
CMIP5	MIROC-miroc5	1.40625° × 1.4°, L40	2.72	6
CMIP5	MIROC-miroc-esm	2.8125° × 2.79°, L80	4.67	14
CMIP5	MOHC-hadgem2-es	1.875° × 1.25°, L38	4.59	12
CMIP5	MPI-esm-lr	1.875° × 1.87°, L47	3.63	9
CMIP5	MRI-cgcm3	1.125° × 1.12°, L48	2.60	10
CMIP5	NCAR-cam5	1.25° × 0.9424°, L30	4.10	9
CMIP5	NCC-noresm1-m	2.5° × 1.8947°, L26	2.80	6

## 2. Data and Methods

We quantify the MBLC fraction changes in response to SST variations at both seasonal and centennial time scales using outputs from 16 models that participated in the World Climate Research Programme's (WCRP's) Coupled Model Intercomparison Project phase 5 (CMIP5) and 11 models from the Coupled Model Intercomparison Project phase 3 (CMIP3) archive. These models (listed in Table 1) are chosen based on the availability of their ECSs from the literature [Gettelman *et al.*, 2012; Andrews *et al.*, 2012; Sherwood *et al.*, 2014; Su *et al.*, 2014]. The model data are downloaded from the Earth System Grid Federation (ESGF) (<http://esgf.org> and <ftp://ftp-esg.ucllnl.org>). This study uses the following variables: "surface temperature," "cloud area fraction at each vertical layer," and "vertical component of velocity." For CMIP5 models, we generate present-day climate from the *historical* run data (except for CNRM-cm5, whose seasonal response is derived using Atmospheric Model Intercomparison Project (AMIP) run because no 3-D cloud fraction is available for its *historical* run) covering 1980–2004 and future climate from the Representative Concentration Pathway 4.5 (RCP4.5) run, the Representative Concentration Pathway (RCP) for the greenhouse gas radiative forcing to reach 4.5 W/m<sup>2</sup> at the end of 21st century, covering 2074–2098 [Taylor *et al.*, 2012]. For the CMIP3 models, we used the *20th Century experiment* for current climate covering period 1970–1999 and *1%/year CO<sub>2</sub> increase experiment to doubling* for climate change scenario ([http://www-pcmdi.llnl.gov/ipcc/standard\\_output.html#Experiments](http://www-pcmdi.llnl.gov/ipcc/standard_output.html#Experiments)).

The observational data include the cloud fraction from the merged CloudSat radar and Cloud-Aerosol Lidar and Infrared Pathfinder Satellite Observations (CALIPSO) data (RL-GEOPROF-LIDAR, version R04) described by Mace *et al.* [2009] and the monthly mean surface temperature measured by Advanced Microwave Scanning Radiometer–Earth Observing System (AMSR-E) (<http://nsidc.org/data/amsrel1a.html>) obtained from the NASA Observations for Model Intercomparison Projects (Obs4MIPs) (<https://www.earthsystemcog.org/projects/obs4mips/>) hosted on the ESGF. We also used the European Centre for Medium-Range Weather Forecasts (ECMWF) ERA-Interim global reanalysis vertical pressure velocity [Dee *et al.*, 2011]. The monthly mean cloud fraction data are produced using the CloudSat/CALIPSO daily cloud fraction data from July 2006 to December 2010 regridded onto a 144 (longitude) × 91 (latitude) × 42 (altitude) grid. The uncertainties

of CloudSat/CALIPSO cloud fraction data are estimated to be 5% with a bias of  $-5$  to  $-7\%$  [Mace *et al.*, 2009; Su *et al.*, 2013; Dolinar *et al.*, 2014], and AMSR-E SST data have a systematic bias of  $\sim 0.03$  K and a standard deviation of  $\sim 0.4$  K [Gentemann *et al.*, 2010]. Additional biases due to undersampled diurnal cycle for A-Train satellites in the monthly mean cloud fraction are estimated to be no more than  $\sim 2\%$  over the tropical oceans [Jiang *et al.*, 2012]. These data have been used for model-observation comparisons [Su *et al.*, 2013; Jiang *et al.*, 2012; Li *et al.*, 2012].

MBLC, topped by the low-level trade inversion, occurs most frequently in large-scale subsidence regions over subtropical oceans [Norris, 1998]. Following Bony and Dufresne [2005], we use the monthly mean midtropospheric (500 hPa) vertical pressure velocity ( $\omega_{500}$ ) to determine large-scale subsidence regions. The MBLC fraction is computed as the total cloud area fraction below 700 hPa over oceans under a random-overlap assumption [Manabe and Strickler, 1964; Ramanathan *et al.*, 1983; Stephens, 1984]. The number of levels below 700 hPa is listed in Table 1. We have also performed the analysis using the maximum-overlap assumption [Stephens, 1984] and found that the results are insensitive to the cloud-overlap assumptions.

To average out interannual variations, we compute a monthly climatology  $\bar{X}$  of a physical quantity  $X$  over  $N$  years in the following way

$$\bar{X}(\text{lon}, \text{lat}, \text{mon}) \equiv \frac{1}{N} \sum_{n=0}^{N-1} X(\text{lon}, \text{lat}, \text{mon} + 12n), \quad \text{mon} = 1, 2, \dots, 12, \quad (1)$$

where (lon, lat) is the longitude and latitude at the center of a grid box and mon labels the month in a year.

This study examines the variations at both seasonal and centennial times scales of averaged MBLC fraction over the oceanic subsidence regions within  $20^\circ\text{N}$ – $40^\circ\text{N}$  and  $20^\circ\text{S}$ – $40^\circ\text{S}$ . The tropical band between  $20^\circ\text{S}$  and  $20^\circ\text{N}$  is excluded for its weak seasonal cycle. The spatial average of  $X$  over these regions is given by

$$\langle \bar{X}(\text{mon}) \rangle \equiv \frac{\sum_{\text{lon}, \text{lat}} X(\text{lon}, \text{lat}, \text{mon}) \cos(\text{lat})}{\sum_{\text{lon}, \text{lat}} \cos(\text{lat})}. \quad (2)$$

To separate MBLC from low-level clouds over convective regions, we further limit the spatial averages to the regions of large-scale subsidence, indicated by  $\omega_{500}$  that changes from month to month. Thus, in equation (2), only grid points with positive  $\omega_{500}$  are included in the spatial averages.

### 3. MBLC Fraction Variation at the Seasonal and Centennial Time Scales

With the methods in the previous section, we computed the seasonal variations and centennial changes of MBLC fraction with changing SST averaged over oceanic subsidence regions within  $20^\circ\text{N}$ – $40^\circ\text{N}$  and  $20^\circ\text{S}$ – $40^\circ\text{S}$  for the 27 models. We also computed corresponding averages of observational MBLC fraction and SST using the CloudSat/CALIPSO cloud fraction, AMSR-E SST, and the ERA-Interim  $\omega_{500}$  from July 2006 through December 2010.

Figure 1 displays the spatial average of MBLC cloud fractions  $\langle \bar{\text{MBLC}}(\text{mon}) \rangle$  for northern (Figure 1a) and southern (Figure 1b) subtropics, respectively, as functions of the underlying averaged SST  $\langle \bar{\text{SST}}(\text{mon}) \rangle$  in each calendar month for current (blue squares) and future (red circles) climate simulated by CMIP5 models. The first 14 subplots are for 14 CMIP5 models (CNRM-cm5 and INM-cm4 are not shown due to not having valid 3-D cloud fraction data for RCP4.5), and the last subplot displays observational data for comparison. The CMIP3 results are similar but not shown for compactness.

Models produce diverse simulations of MBLC: the overall range is 20%–65% (30%–75%) for northern (southern) hemisphere compared with the observation's 35%–50% (45%–55%). It is clear that MBLC is not uniquely determined by SST; other factors like seasonal variations of circulation, water vapor amount, lower tropospheric stability, or estimated inversion strength (EIS) also affect the amount of MBLC [Qu *et al.*, 2014]. This is especially true for northern hemisphere, where a hysteresis behavior shows in the MBLC–SST relations for all the models and the observations. For southern hemisphere, models CCCMA-canesm2, GFDL-cm3, IAP-fgoal-g2, MIROC-esm, MIROC-miroc5, MOHC-hadgem2-es, and NCAR-cam5 and the observations all show that the average of MBLC over subsidence oceans in  $20^\circ\text{S}$ – $40^\circ\text{S}$  is mainly determined by the

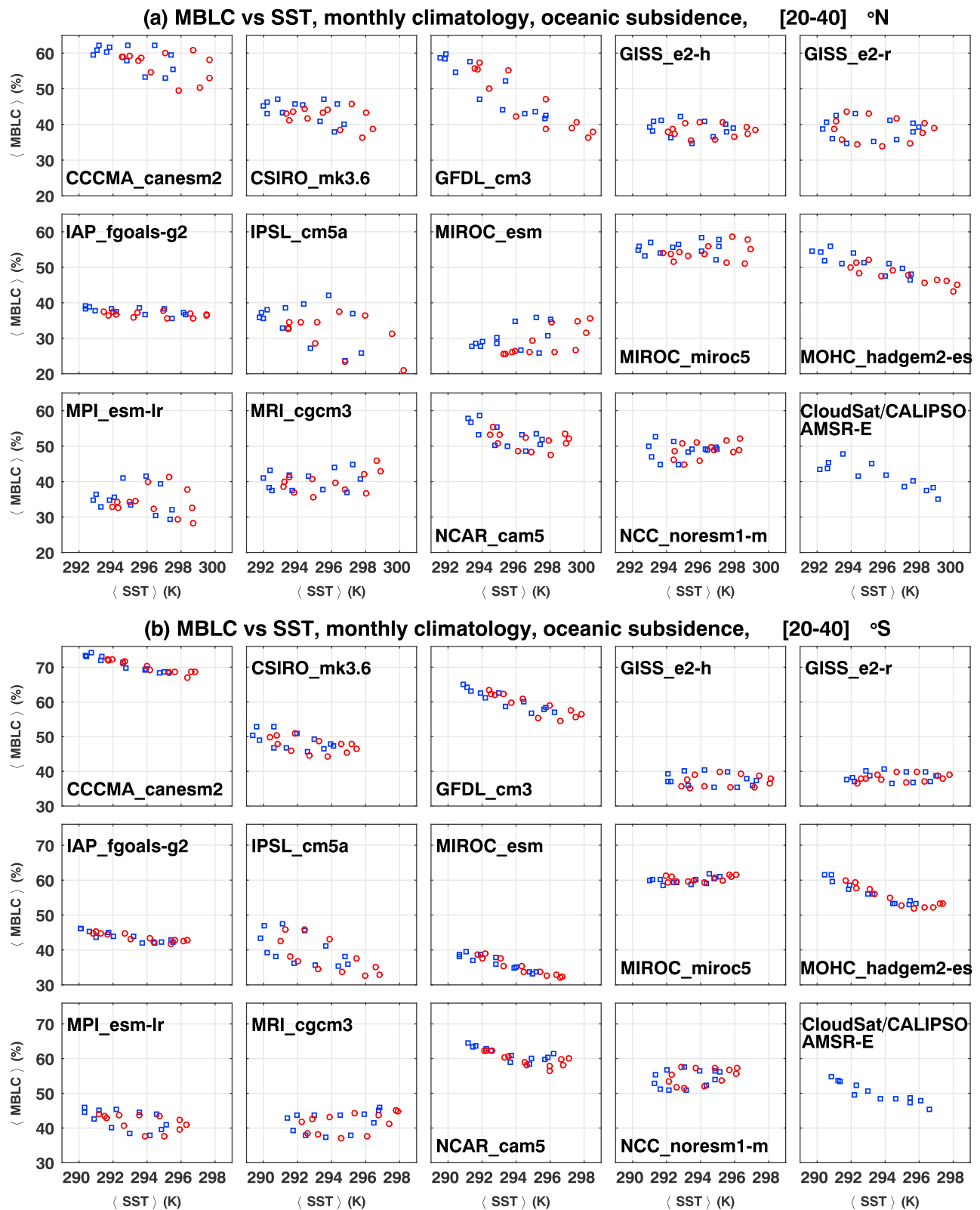


**Figure 1.** Seasonal variations of MBLC fraction averaged over oceanic subsidence regions within (a) 20°N–40°N and (b) 20°S–40°S as function of averaged underlying SST for both current and future climate. The first 14 subplots are for 14 GCMs from CMIP5, and the last subplot shows the seasonal variations of observed MBLC derived from 4 year CloudSat/CALIPSO MBLC cloud fraction as a function of averaged SST measured by AMSR-E. Blue squares and red circles represent present and future climate, respectively.

corresponding SST. For the rest of models, the MBLC fractions still have significant dependency on physical quantities other than SST. The different seasonal MBLC-SST relations among the models and observations demonstrate that current GCMs do not simulate MBLC consistently.

Despite the differences and complexities, in general, the averaged MBLC fraction bears an approximately linear relationship with SST on seasonal time scale in all models and the observations. We will focus on this overall correlation and will not examine the cause and effect of the interaction between MBLC and SST. Majority of the models agree with the observation, showing a decreasing MBLC fraction with increasing SST (negative slope) in both hemispheres.

Interestingly, the seasonal cycle of MBLC in the future climate is an evident shift from the current seasonal cycle; i.e., the future seasonal variation with SST is at the same rate as the current climate except a shift in the mean temperature associated with global warming. For most of the models, the future climate shifts from the current climate along the overall trend of the seasonal variation, i.e., the overall seasonal variation is aligned with the shift of the MBLC under global warming.

We define the seasonal MBLC fraction response to SST change as the regression slope  $\alpha_{\text{season}}$  between  $\langle \text{MBLC}(\text{mon}) \rangle$  and  $\langle \text{SST}(\text{mon}) \rangle$  over the 12 months via

$$\langle \text{MBLC}(\text{mon}) \rangle = \alpha \langle \text{SST}(\text{mon}) \rangle + \beta, \quad \text{mon} = 1, 2, \dots, 12. \quad (3)$$

The centennial scale MBLC fraction response to surface warming for a calendar month (mon) of a year is computed as the ratio of the change of  $\langle \text{MBLC}(\text{mon}) \rangle$  from current to future climate,

$$\Delta \langle \text{MBLC}(\text{mon}) \rangle = \langle \text{MBLC}(\text{mon}) \rangle_{\text{future}} - \langle \text{MBLC}(\text{mon}) \rangle_{\text{present}}$$

to the change of  $\langle \text{SST}(\text{mon}) \rangle$

$$\Delta \langle \text{SST}(\text{mon}) \rangle = \langle \text{SST}(\text{mon}) \rangle_{\text{future}} - \langle \text{SST}(\text{mon}) \rangle_{\text{present}}.$$

The mean centennial scale MBLC fraction response to surface warming  $\alpha_{\text{century}}$  is the average of the MBLC fraction responses for all 12 months of a year,

$$\alpha_{\text{century}} = \frac{1}{12} \sum_{\text{mon}=1}^{12} \frac{\Delta \langle \text{MBLC}(\text{mon}) \rangle}{\Delta \langle \text{SST}(\text{mon}) \rangle}. \quad (4)$$

The seasonal MBLC fraction response  $\alpha_{\text{season}}$  and centennial responses  $\alpha_{\text{century}}$  are computed for 16 CMIP5 and 11 CMIP3 models, separately for both hemispheres. Figure 2 displays the relationships between the seasonal and centennial MBLC fraction response to SST in northern (Figure 2a) and southern (Figure 2b) hemispheres. The intermodel variations of the response sensitivities  $\alpha_{\text{season}}$  and  $\alpha_{\text{century}}$  are well correlated with correlation of 0.6 (0.73) for northern (southern) hemisphere, above the 99.9% statistical significance threshold  $\sim 0.59$  for 25 models (for future climate, the cloud fraction of INM-cm4 is unphysically large and CNRM-cm5 does not output 3-D cloud fraction). Because the models are not completely independent as noted by Knutti *et al.* [2013], we adopt a bootstrap method [Efron, 1979] to compute empirical probability distributions of the correlations between  $\alpha_{\text{season}}$  and  $\alpha_{\text{century}}$  for both hemispheres using 40,000 samples generated by randomly drawing models from the 25 models. Figures 2c and 2d display the estimated empirical probability density functions of the correlation, which show that correlation values are mostly between 0.4 and 0.9 (0.6 and 0.9) for northern (southern) hemisphere. There is no negative correlation in the 40,000 samples giving a very high confidence of positive correlation. The double-peak for northern hemisphere is due to model 3, which behaves like an outlier; had we excluded it, the correlation would have been 0.72. Two vertical dashed green lines mark the correlation values 0.57 (0.43) and 0.49 (0.31) at which the cumulative probability from the left is respectively 0.01 and 0.001 for the northern (southern) hemisphere. The identity function  $y=x$  is shown in Figures 2a and 2b, indicating that  $\alpha_{\text{season}}$  and  $\alpha_{\text{century}}$  are close to each other in magnitude, especially for southern hemisphere.

The linkage between the seasonal and centennial changes of MBLC fraction with SST is not surprising because the typical response time of MBLC to external forcing is much smaller than a month [Garraff, 1992]. Hence, seasonal sensitivity  $\alpha_{\text{season}}$  can serve as a proxy for the long-term response  $\alpha_{\text{century}}$ , which is intimately related to the low cloud feedback and thus the model climate sensitivity [e.g., Bony and Dufresne, 2005;

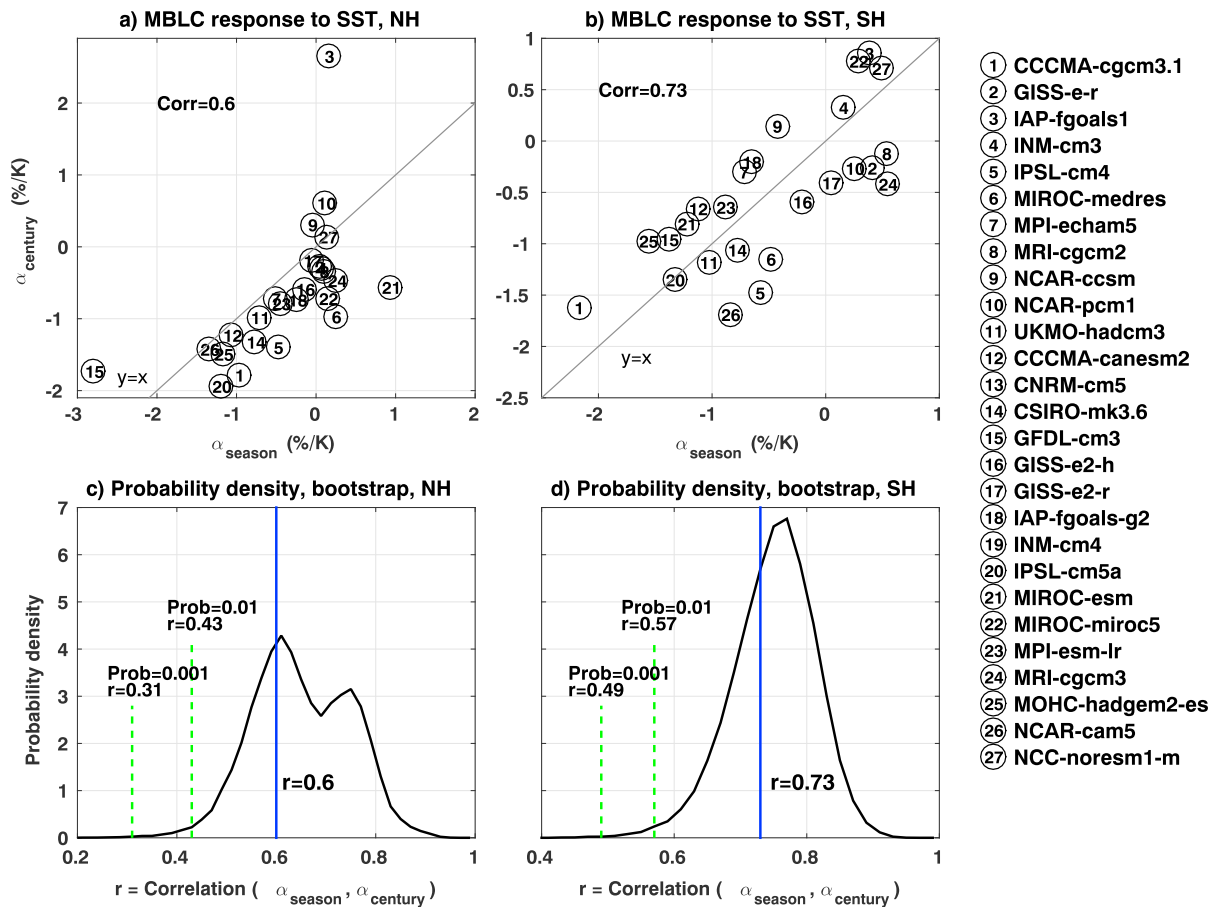


**Figure 2.** Sensitivities of averaged MBLC response to SST at centennial time scale ( $\alpha_{\text{century}}$ ) versus seasonal scale ( $\alpha_{\text{season}}$ ) for the oceanic subsidence region in (a) 20°N–40°N and (b) 20°S–40°S, respectively, for the 25 models (CNRM-cm5 and INM-cm4 are not shown due to not having valid 3-D cloud fraction data for future climate). The correlations and the  $y=x$  line are shown. (c and d) Empirical probability density functions of the correlations between  $\alpha_{\text{century}}$  and  $\alpha_{\text{season}}$  in northern and southern hemispheres estimated using a bootstrap method. Green vertical lines mark the correlations at which the cumulative probabilities from the left side are 0.001 and 0.01, respectively. Blue vertical lines mark the correlations for using all the 25 models as shown in Figures 2a and 2b.

Clement *et al.*, 2009; Zelinka *et al.*, 2012; Fasullo and Trenberth, 2012; Sherwood *et al.*, 2014; Su *et al.*, 2014]. It is also interesting that the sensitivities  $\alpha_{\text{season}}$  and  $\alpha_{\text{century}}$  for northern hemisphere are similar to those for southern hemisphere; the values for both hemispheres are well correlated across different models with confidence level above 99.9% (see supporting information for more details).

#### 4. Correlation With ECS and Observational Constraints

Previous studies [Bony and Dufresne, 2005; Andrews *et al.*, 2012; Zelinka *et al.*, 2012] showed that the boundary layer could feedback explained most of the spread in ECS. Therefore, the MBLC fraction response to SST, critical to shortwave cloud feedback, is expected to be correlated with model ECS. Figure 3a confirms this: the intermodel variation of  $\alpha_{\text{century}}$  (average of both hemispheres) is well correlated with ECS with a correlation of  $-0.69$ . The greater reduction of MBLC fraction leads to a higher ECS. Similarly,  $\alpha_{\text{season}}$  is also well correlated with model ECS. The intermodel spread in  $\alpha_{\text{season}}$  explains about 41% variance of intermodel spread in ECS with a correlation coefficient of  $-0.64$  (Figure 3b). Statistically, the probability for  $\alpha_{\text{century}}$  ( $\alpha_{\text{season}}$ ) and ECS being negatively correlated is greater than 99.9% assuming that models are independent. Figure 3c (Figure 3d) displays the probability density function of the correlation between  $\alpha_{\text{century}}$  ( $\alpha_{\text{season}}$ ) and ECS estimated from the bootstrap method with randomly drawing of 40,000 samples showing that correlation  $-0.68$  ( $-0.64$ ) is near the center of the distribution with 99% confidence to have correlation  $< -0.47$  ( $-0.37$ ) and with 99.9% confidence to have correlation  $< -0.37$  ( $-0.27$ ) as marked by the green lines. For this



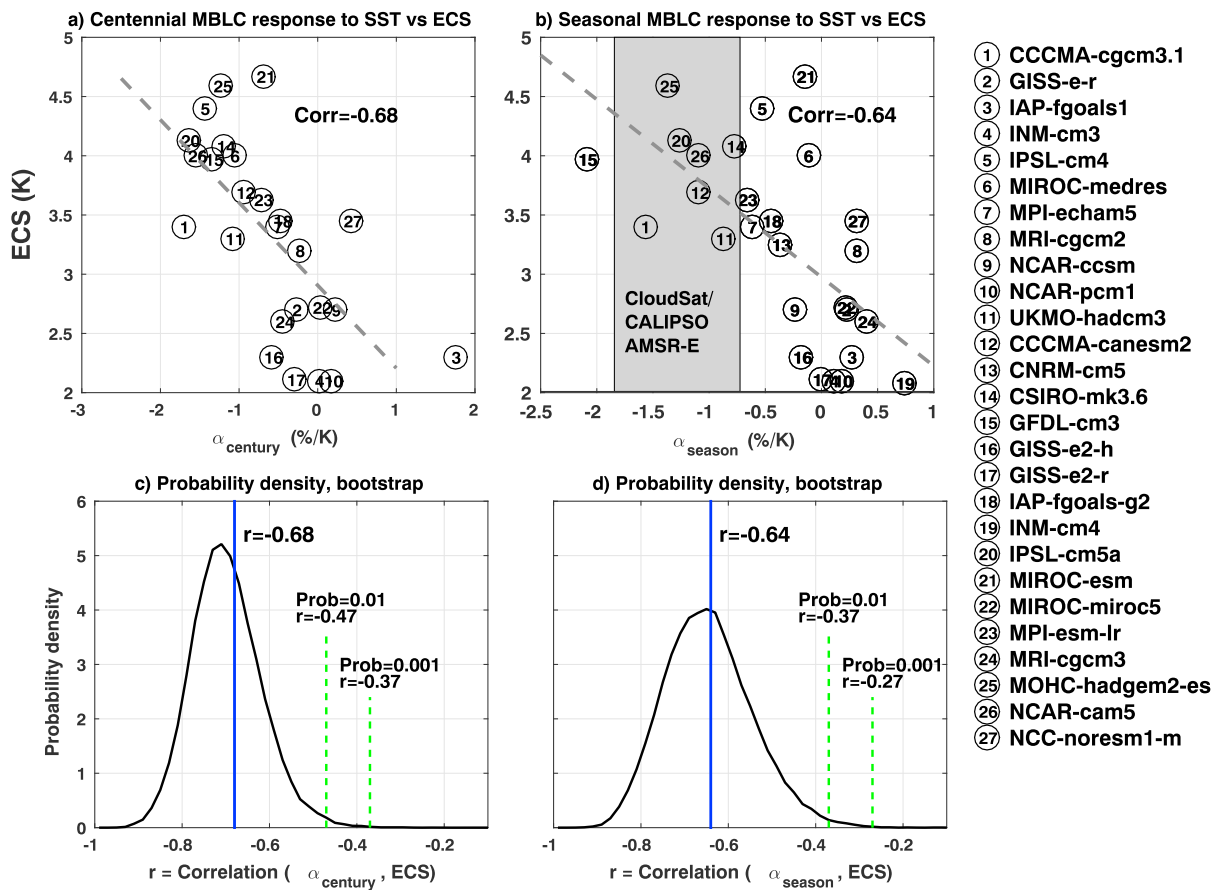


**Figure 3.** Relations between model ECSs and MBLC response sensitivities to SST change at (a) centennial scale  $\alpha_{\text{century}}$  and (b) seasonal scale  $\alpha_{\text{season}}$ . (c and d) Empirical probability density functions for the  $\alpha_{\text{century}}$ -ECS correlation and  $\alpha_{\text{season}}$ -ECS correlation, respectively, as estimated using the bootstrap method. The gray area in Figure 3b marks the observed MBLC response sensitivity using CloudSat/CALIPSO cloud fraction data and AMSR-E SST data with the uncertainties ( $\pm 3\sigma$ ). Green vertical lines mark the correlations at which the cumulative probabilities from the right side are 0.001 and 0.01, respectively. Blue vertical lines mark the correlations for using all the available models as shown in Figures 3a and 3b.

correlation, MBLC response at seasonal scale  $\alpha_{\text{season}}$  provides a metric of shortwave cloud radiative feedback and opens a new way to constrain model climate sensitivity using temporal variabilities in current climate, different from previous studies that focused on current climate means [Fasullo and Trenberth, 2012; Sherwood et al., 2014; Su et al., 2014; Tian, 2015].

We compute the observed  $\alpha_{\text{season}}$  using CloudSat/CALIPSO cloud fraction and AMSR-E SST. The uncertainty of  $\alpha_{\text{season}}$  is estimated as the year-to-year standard deviation of  $\alpha_{\text{season}}$  for the 4 years from 2006 to 2010, which include two EL Niños and two La Niñas [Su and Jiang, 2013]. The larger value out of the northern and southern hemispheres is used for the uncertainty estimate. Shown in Figure 3b, the gray area represents  $\pm 3\sigma$  (standard error) (0.56%/K) around the observed  $\alpha_{\text{season}}$  of  $-1.28$  K. Model seasonal responses  $\alpha_{\text{season}}$  has a range from  $-2.1$  to  $0.73\%/K$  with 18 models capturing the decreasing MBLC with SST. Seven models, namely, CCCMA-cgcm3.1, UKMO-hadcm3, CCCMA-canesm2, CSIRO-mk3.6, IPSL-cm5a, NCAR-cam5, and MOHC-hadgem2-es, have seasonal MBLC response to SST consistent with the observations. Assuming that these models produce a realistic low cloud radiative feedback, the “best estimate” of ECS has a mean of  $3.9$  K with a standard deviation of  $0.45$  K. This best estimate of ECS is larger than the multimodel-mean of  $3.3$  K and has a much smaller standard deviation than  $0.81$  K from the 27 models, consistent with previous studies [Fasullo and Trenberth, 2012; Sherwood et al., 2014; Tsushima et al., 2013; Su et al., 2014; Tian, 2015]. Similar results hold if we use the AMIP experiments to estimate seasonal response  $\alpha_{\text{season}}$ .

While the result of a higher ECS is consistent with previous studies, this study is unique in that (1) it uses the temporal variabilities of current climate instead of the mean state; (2) it uses the seasonal MBLC fraction

response to SST, which is directly related to the low cloud feedback, to constraint the ECS, and hence provides a clearer physical meaning than other proxies. Because accurate observational record of MBLC fraction is rather short, the robust seasonal variation of MBLC fraction with SST becomes an attractive metric for model evaluation and constraint of ECS.

## 5. Conclusions

Using model simulations from 27 climate models, we estimate the MBLC fraction response to surface warming over oceanic subsidence regions within 20°N–40°N and 20°S–40°S at both seasonal and centennial (climate change) time scales. We find that MBLC fraction response to SST warming at seasonal and centennial scales is strongly correlated as in the case of snow albedo feedback [Hall and Qu, 2006]. Therefore, for the MBLC, seasonal response can be a proxy for the response under global warming in these models. Because the model climate sensitivity differences are primarily caused by the differences in simulating the shortwave radiative feedback from the MBLC, the intermodel spread in the seasonal MBLC response is strongly correlated with that in ECS. Using CloudSat/CALIPSO cloud fraction and AMSR-E SST, we find the models that simulate a seasonal MBLC response to SST consistent with the observation yield an ensemble-mean ECS of 3.9 K, about 0.6 K higher than the multimodel-mean ECS from all the 27 models analyzed. Our results support the previous studies that favor the high ECS and underscore the importance of MBLC variations to climate feedback.

## Acknowledgments

We thank Mark Zelinka and Joel Norris for their useful discussions and the two anonymous reviewers for their constructive suggestions to improve the manuscript. This work is conducted at JPL/Caltech under a contract with NASA, supported by the ROSES NDOA, MAP, and NEWS programs. The model data are downloaded from the ESGF (<http://esgf.org> and <ftp://ftp-esg.ucllnl.org>). We acknowledge the modeling groups, the Program for Climate Model Diagnosis and Intercomparison and the WGCM, for their roles in making available the WCRP CMIP3/CMIP5 multimodel data set. Support of this data set is provided by the Office of Science, U.S. DOE. The merged CloudSat radar and CALIPSO lidar data (RL-GEOPROF-LIDAR, version R04) are downloaded from <http://www.cloudsat.cira.colostate.edu/data-products/>, and the monthly mean SST measured by AMSR-E is obtained from the Obs4MIPs project (<https://www.earthsystemcog.org/projects/obs4mips/>) hosted on the ESGF. The ERA-Interim global reanalysis vertical velocity data are downloaded from the ECMWF data server via <http://www.ecmwf.int/en/research/climate-reanalysis/era-interim>.

## References

- Andrews, T., M. J. Webb, and K. E. Taylor (2012), Forcing, feedbacks and climate sensitivity in CMIP5 coupled atmosphere-ocean climate models, *Geophys. Res. Lett.*, **39**, L09712, doi:10.1029/2012GL051607.
- Arrhenius, S. (1896), On the influence of carbonic acid in the air upon the temperature of the ground, *Philos. Mag.*, **41**, 237–276.
- Bony, S., and J.-L. Dufresne (2005), Marine boundary layer clouds at the heart of tropical cloud feedback uncertainties in climate models, *Geophys. Res. Lett.*, **32**, L20806, doi:10.1029/2005GL023851.
- Callendar, G. S. (1938), The artificial production of carbon dioxide and its influence on temperature, *Q. J. R. Meteorol. Soc.*, **64**, 223–240.
- Cess, R. D., et al. (1990), Intercomparison and interpretation of climate feedback processes in 19 atmospheric general circulation models, *J. Geophys. Res.*, **95**, 16,601–16,615, doi:10.1029/JD095iD10p16601.
- Charney, J. G., et al. (1979), *Carbon Dioxide and Climate: A Scientific Assessment*, pp. 22, National Academy of Science.
- Clement, A. C., R. Burgman, and J. R. Norris (2009), Observational and model evidence for positive low-level cloud feedback, *Science*, **325**, 460–464.
- Dee, D. P., et al. (2011), The ERA-Interim reanalysis: Configuration and performance of the data assimilation system, *Q. J. R. Meteorol. Soc.*, **137**, 553–597.
- Dessler, A. (2010), A Determination of the cloud feedback from climate variations over the past decade, *Science*, **330**, 1523–1527.
- Dolinar, E. K., X. Dong, B. Xi, J. H. Jiang, and H. Su (2014), Evaluation of CMIP5 simulated clouds and TOA radiation budgets using NASA satellite observations, *Clim. Dyn.*, **44**(7–8), 2229–2247, doi:10.1007/s00382-014-2158-9.
- Efron, B. (1979), Bootstrap methods: Another look at the jackknife, *Ann. Stat.*, **7**, 1–26.
- Fasullo, J. T., and K. E. Trenberth (2012), A less cloudy future: The role of subtropical subsidence in climate sensitivity, *Science*, **338**, 792–794.
- Garratt, J. R. (1992), *The Atmospheric Boundary Layer*, Cambridge Univ. Press, Cambridge, U. K.
- Gentemann, C. L., F. J. Wentz, M. Brewer, K. Hilburn, and D. Smith (2010), Passive microwave remote sensing of the ocean: An overview, in *Oceanography from Space, Revisited*, edited by V. Barale, J. F. R. Gower, and L. Alberotanza, pp. 13–33, Springer, Heidelberg.
- Gettelman, A., J. E. Kay, and K. M. Shell (2012), The evolution of climate sensitivity and climate feedbacks in the Community Atmosphere Model, *J. Clim.*, **25**, 1453–1469.
- Hall, A., and X. Qu (2006), Using the current seasonal cycle to constrain snow albedo feedback in future climate change, *Geophys. Res. Lett.*, **33**, L03502, doi:10.1029/2005GL025127.
- Jiang, J. H., et al. (2012), Evaluation of cloud and water vapor simulations in CMIP5 climate models using NASA “A-Train” satellite observations, *J. Geophys. Res.*, **117**, D14105, doi:10.1029/2011JD017237.
- Klein, S. A., and D. L. Hartmann (1993), The seasonal cycle of low stratiform clouds, *J. Clim.*, **6**, 1587–1606.
- Klein, S., Y. Zhang, M. D. Zelinka, R. Pincus, J. Boyle, and P. J. Gleckler (2013), Are climate model simulations of clouds improving? An evaluation using the ISCCP simulator, *J. Geophys. Res. Atmos.*, **18**, 1329–1342, doi:10.1002/jgrd.50141.
- Knutti, R., D. Masson, and A. Gettelman (2013), Climate model genealogy: Generation CMIP5 and how we got there, *Geophys. Res. Lett.*, **40**, 1194–1199, doi:10.1002/grl.50256.
- Li, J.-L. F., et al. (2012), An observationally based evaluation of cloud ice water in CMIP3 and CMIP5 GCMs and contemporary reanalyses using contemporary satellite data, *J. Geophys. Res.*, **117**, D16105, doi:10.1029/2012JD017640.
- Mace, G. G., Q. Zhang, M. Vaughan, R. Marchand, G. Stephens, C. Trepte, and D. Winker (2009), A description of hydrometeor layer occurrence statistics derived from the first year of merged CloudSat and CALIPSO data, *J. Geophys. Res.*, **114**, D00A26, doi:10.1029/2007JD009755.
- Manabe, S., and R. Strickler (1964), Thermal equilibrium of the atmosphere with a convective adjustment, *J. Atmos. Sci.*, **21**, 361–385.
- Meehl, G. A., et al. (2007), Global climate projections, in *Climate Change 2007: The Physical Science Basis. Contribution of Working Group I to the Fourth Assessment Report of the Intergovernmental Panel on Climate Change*, edited S. Solomon et al., pp. 747–845, Cambridge Univ. Press, Cambridge, U. K.
- Norris, J. R. (1998), Low cloud type over the ocean from surface observations. Part II: Geographical and seasonal variations, *J. Clim.*, **11**, 383–403.
- Qu, X., A. Hall, S. A. Klein, and P. M. Caldwell (2014), On the spread of changes in marine low cloud cover in climate model simulations of the 21st century, *Clim. Dyn.*, **42**(9–10), 2602–2606, doi:10.1007/s00382-013-1945.



- Ramanathan, V., E. J. Pitcher, R. C. Malone, and M. L. Blackmon (1983), The response of a spectral general circulation model to refinement in radiative process, *J. Atmos. Sci.*, *40*, 605–630.
- Sherwood, S. C., S. Bony, and J.-L. Dufresne (2014), Spread in model climate sensitivity traced to atmospheric convective mixing, *Nature*, *505*, 37–42.
- Stephens, G. L. (1984), The parameterization of radiation of numerical weather prediction and climate model, *Mon. Weather Rev.*, *112*, 826–867.
- Stocker, T. F., et al. (Eds.) (2013), Climate phenomena and their relevance for future regional climate change, in *Climate Change 2013: The Physical Science Basis. Contribution of Working Group I to the Fifth Assessment Report of the Intergovernmental Panel on Climate Change*, edited by T. F. Stocker, 1535 pp., Cambridge Univ. Press, Cambridge, U. K., and New York, doi:10.1017/CBO9781107415324.
- Su, H., and J. H. Jiang (2013), Tropical clouds and circulation changes during the 2006–07 and 2009–10 El Niños, *J. Clim.*, *26*(2), 399–413.
- Su, H., et al. (2013), Diagnosis of regime-dependent cloud simulation errors in CMIP5 models using “A-Train” satellite observations and reanalysis data, *J. Geophys. Res. Atmos.*, *118*, 2762–2780, doi:10.1029/2012JD018575.
- Su, H., J. H. Jiang, C. Zhai, T. J. Shen, J. D. Neelin, G. L. Stephens, and Y. L. Yung (2014), Weakening and strengthening structures in the Hadley Circulation change under global warming and implications for cloud response and climate sensitivity, *J. Geophys. Res. Atmos.*, *119*, 5787–5805, doi:10.1002/2014JD021642.
- Taylor, K. E., R. J. Stouffer, and G. A. Meehl (2012), A summary of the CMIP5 experiment design, *Bull. Am. Meteorol. Soc.*, *93*, 485–498.
- Tian, B. J. (2015), Spread of model climate sensitivity linked to double-intertropical convergence zone bias, *Geophys. Res. Lett.*, *42*, 4133–4141, doi:10.1002/2015GL064119.
- Tsushima, Y., M. Ringer, M. Webb, and K. Williams (2013), Quantitative evaluation of the seasonal variations in climate model cloud regimes, *Clim. Dyn.*, *41*, 2679.
- Zelinka, M., S. Klein, and D. Hartmann (2012), Computing and partitioning cloud feedbacks using cloud property histograms. Part I: Cloud radiative kernels, *J. Clim.*, *25*, 3715–3735.